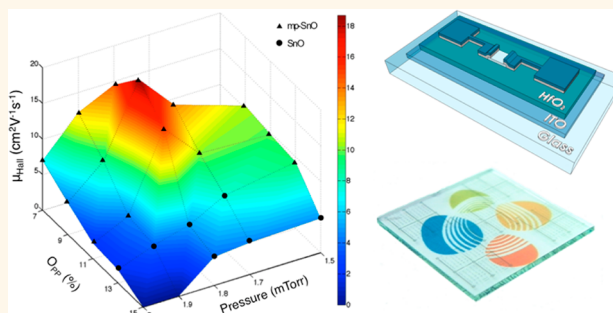


Record Mobility in Transparent p-Type Tin Monoxide Films and Devices by Phase Engineering

Jesus A. Caraveo-Frescas,[†] Pradipta K. Nayak,[†] Hala A. Al-Jawhari,[‡] Danilo B. Granato,[†] Udo Schwingenschlögl,[†] and Husam N. Alshareef^{†,*}

[†]Materials Science and Engineering, King Abdullah University of Science & Technology (KAUST), Thuwal 23955-6900, Saudi Arabia, and [‡]Department of Physics, King Abdulaziz University, Jeddah 21589, Saudi Arabia

ABSTRACT Here, we report the fabrication of nanoscale (15 nm) fully transparent p-type SnO thin film transistors (TFT) at temperatures as low as 180 °C with record device performance. Specifically, by carefully controlling the process conditions, we have developed SnO thin films with a Hall mobility of 18.71 cm² V⁻¹ s⁻¹ and fabricated TFT devices with a linear field-effect mobility of 6.75 cm² V⁻¹ s⁻¹ and 5.87 cm² V⁻¹ s⁻¹ on transparent rigid and translucent flexible substrates, respectively. These values of mobility are the highest reported to date for any p-type oxide processed at this low temperature. We further demonstrate that this high mobility is realized by careful phase engineering. Specifically, we show that phase-pure SnO is not necessarily the highest mobility phase; instead, well-controlled amounts of residual metallic tin are shown to substantially increase the hole mobility. A detailed phase stability map for physical vapor deposition of nanoscale SnO is constructed for the first time for this p-type oxide.



KEYWORDS: p-type oxide · tin monoxide · thin-film transistors

Oxide semiconductors hold great promise as materials for use in many emerging electronic applications. Such applications include transparent and flexible displays, sensor arrays, flexible solar cells, and logic circuitry for so-called invisible electronics.^{1–3} The use of oxide-based thin-film transistors (TFT) has already been shown as a good solution to the increasingly demanding requirements of better display technologies.^{4,5} For example, transparent amorphous In–Ga–Zn–O with a mobility of 10 cm² V⁻¹ s⁻¹ has been demonstrated to be useful in switching/driving TFTs in the next generation of flat panel and flexible displays.² Outstanding TFT results have been reported for display applications based on various oxide-based semiconducting films,⁶ although all such materials are based on n-type semiconductors. A p-type oxide with comparable performance (mobility, current-carrying capacity, optical transparency and mechanical flexibility) to that of previously developed n-type transparent semiconducting oxides not

only will allow the realization of better display technologies but also will usher in a new era of transparent electronics.

Electronic circuits based on single crystalline silicon substrates have limited potential applications in large-area electronics because of their opacity, high processing temperatures, and rigidity especially when mechanical flexibility is desired. The use of amorphous silicon has partially addressed this issue, but its field-effect mobility of $\mu_{FE} \leq 1$ cm² V⁻¹ s⁻¹ limits its performance.⁷ Moreover, low-temperature processing is essential to fabricating flexible devices on inexpensive plastic substrates.⁸ One group of candidate materials to satisfy this requirement is organic semiconductors, but their μ_{FE} is barely different from that of amorphous silicon.⁹ Recently, n-type oxide semiconductors, with high optical transparency, low-temperature processing, and performance comparable to that of polycrystalline silicon, have been demonstrated using a variety of deposition methods.^{10–12}

* Address correspondence to husam.alshareef@kaust.edu.sa.

Received for review February 20, 2013 and accepted May 6, 2013.

Published online May 13, 2013
10.1021/nn400852r

© 2013 American Chemical Society

The limiting factor for the full integration of oxide-based devices, however, continues to be the development of a p-type oxide material with performance comparable to that of the n-type oxides. Cu-based oxides have been demonstrated to exhibit p-type behavior.^{13,14} The best performance ($\mu_{FE} = 4.3 \text{ cm}^2 \text{ V}^{-1} \text{ s}^{-1}$)¹⁵ has been exhibited when Cu_2O is deposited at 500 °C. Despite their high hole mobility, Cu_2O -based oxides are of limited use because its optical transparency is hindered by their low optical bandgap of 2.2 eV.^{16,17} If plastic and other flexible substrates are the ultimate goal, low processing temperatures are essential. Recently, devices based on p-type tin monoxide (SnO) have been developed, but again their use is limited by either high deposition temperatures or low μ_{FE} similar to a-Si:H.^{18–23} Not even Hall-effect mobility (μ_{Hall}) in the range of n-type amorphous oxide semiconductors² ($10 \text{ cm}^2 \text{ V}^{-1} \text{ s}^{-1}$) has been reported for SnO , preventing its use in practical applications.

RESULTS AND DISCUSSION

Film Characterization. The pathway to achieve high mobility involved a large number of experimental studies, each repeated several times, in which we carefully mapped out a very wide process window in our reactive DC magnetron sputtering process. It is known that Sn metal occurs in two possible oxidation states (2^+ and 4^+), with SnO_2 (4^+) being the most thermodynamically stable phase.²⁴ SnO is a metastable phase that easily oxidizes to n-type SnO_2 . It is also known that depositing the correct p-type phase of SnO by physical vapor deposition is challenging due to the required fine control of oxygen pressure to prevent the formation of SnO_2 or any other intermediate phases such as Sn_2O_3 or Sn_3O_4 with n-type characteristics.²⁴ In our extensive experimental studies, we have found that the p-type transport in tin monoxide occurs only in a very narrow window of deposition conditions. This window occurs when the relative oxygen partial pressure (O_{PP}) [where $O_{PP} = P_{O_2}/(P_{O_2} + P_{Ar})$] and deposition pressure (P) lie within the process boundaries illustrated by the bold black lines in Figure 1a. Specifically, p-type tin monoxide transport occurs in the process regime where $7\% \leq O_{PP} \leq 15\%$ and $1.5 \text{ mTorr} \leq P \leq 2 \text{ mTorr}$. For the case where P is $>2.0 \text{ mTorr}$ or $O_{PP} > 15\%$, either amorphous phase or SnO_2 is formed. Pan and Fu have shown that in the presence of excess oxygen (and temperature), the metastable SnO phase transforms to SnO_2 via a process initiated by the local disproportionate redistribution of internal oxygen,²⁵ known as the disproportionation mechanism.²⁶ In the first step of the oxidation process the metastable SnO phase coexists with intermediate products such as Sn_3O_4 and Sn, then the inward diffusion of external oxygen causes the full oxidation into the thermodynamically stable SnO_2 phase.^{24–26} In our films, the observation of an amorphous phase when $P > 2.0 \text{ mTorr}$ and $15\% \leq O_{PP}$

$< 20\%$ indicates that at these conditions the oxygen concentration is high enough not to form p-type SnO , but the thermal budget is not enough to crystallize the intermediate product (Sn_3O_4), or its diffraction intensity is too low to be detected by our tool. At higher O_{PP} ($>20\%$) oxygen content is enough to directly crystallize the films into SnO_2 phase after annealing. When $O_{PP} < 7\%$ and/or $P < 1.5 \text{ mTorr}$, metallic tin ($\beta\text{-Sn}$) is the dominant phase and the films exhibit either metallic or weak n-type conduction. In this study, all the samples were deposited at room temperature following a postannealing treatment in air, in a tube furnace at 180 °C for 30 min.

The X-ray diffraction (XRD) patterns in Figure 1b show the dependence of phase formation on the oxygen partial pressure (O_{PP}) at a deposition pressure (P) of 1.8 mTorr, as an example (in fact, similar XRD analysis was done for many deposition pressures to construct the phase map in Figure 1a). As indicated in Figure 1b, films deposited at $7\% \leq O_{PP} \leq 11\%$ show the presence of small traces of $\beta\text{-Sn}$ in a matrix of SnO (this mixture is henceforth referred to as mixed phase SnO or **mp-SnO**), while films deposited at $13\% \leq O_{PP} \leq 15\%$ comprise pure tetragonal SnO . The Sn metal was uniformly distributed in the SnO matrix as seen in plane view transmission electron microscopy and as reflected by the excellent device uniformity, which will be discussed later on. Films deposited at higher O_{PP} form either amorphous SnO phase (*a-SnO*) (e.g., 17% O_{PP}) or SnO_2 (e.g., 20% O_{PP}). Further, we found that the tin oxide phase formation (SnO , mp-SnO, *a-SnO*, or SnO_2) is *extremely sensitive* to the deposition pressure. Figure 1c shows the influence of the deposition pressure on the SnO phase formation at 13% O_{PP} . A pure polycrystalline SnO phase is obtained in the deposition pressure range of 1.7 mTorr to 2.0 mTorr. As the deposition pressure increases, the intensity of the SnO diffraction peaks increases up to $P = 1.8 \text{ mTorr}$ and then decreases at $P = 1.9 \text{ mTorr}$ to completely vanish at $P \geq 2.0 \text{ mTorr}$, indicating the formation of amorphous films. The O_{PP} is not only crucial to control which oxide phase will form, but also to control the amount of metallic tin present in the films. Figure 1d shows XRD patterns in a narrower 2θ range to clarify how the diffraction intensity of the $\beta\text{-Sn}$ decreases as a function of O_{PP} at 1.8 mTorr, which turned out to be the optimal deposition pressure for device performance as discussed below. X-ray photoelectron spectroscopy (XPS) analysis was used to estimate the metallic tin content in the mp-SnO films. For the 1.8 mTorr deposition pressure, as the relative oxygen partial pressure (O_{PP}) was reduced from 15% to 7%, the amount of metallic tin in the films increased from undetectable by XPS to nearly 5 atom %.

Noticeable differences in the intensities of the (101) and (110) diffraction peaks are observed with increasing O_{PP} (Figure 1b). The difference in intensities of the

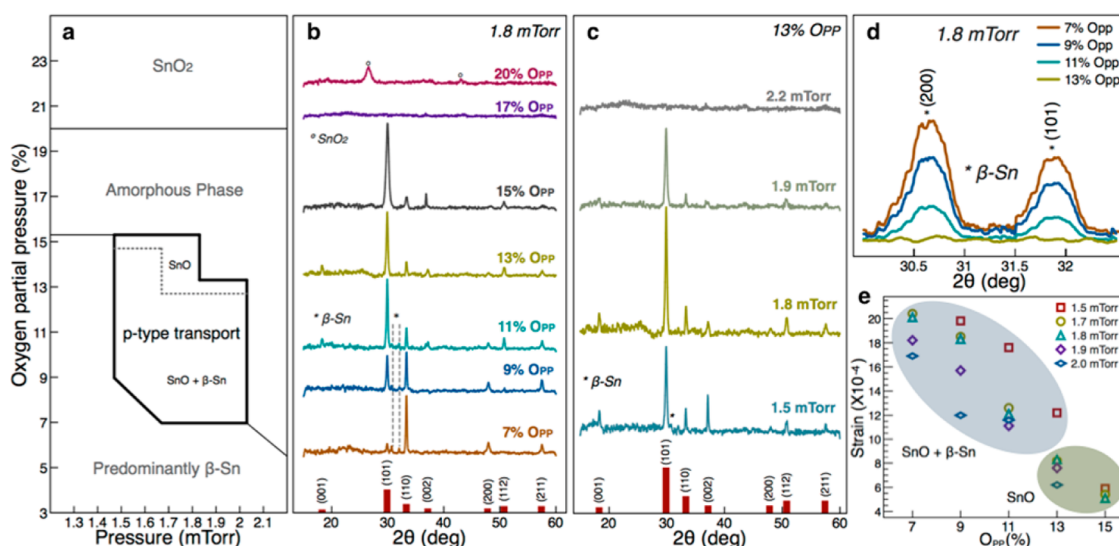


Figure 1. (a) Phase stability map to obtain p-type tin monoxide, which occurs in a very narrow window of deposition conditions; (b) XRD patterns showing phase formation dependence on the oxygen partial pressure (O_{pp}) at a deposition pressure of 1.8 mTorr; (c) XRD patterns showing deposition pressure dependence of the SnO phase at 13% O_{pp} . The red lines at the bottom show the diffraction pattern (JCPDS card No. 06-0395) of tetragonal SnO. (d) The zoom in XRD patterns showing the presence of β -Sn in SnO films decreases as the O_{pp} increases and pure SnO films are obtained at 13% O_{pp} ; (e) lattice strain for all deposition conditions calculated from the XRD patterns. Higher strain values are observed for the mixed phase SnO films (SnO + β -Sn), indicating the presence of lattice impurities.

XRD peaks can have many origins, such as crystallite size, lattice defects, and preferential crystallite orientation.^{27–29} We have identified preferential crystallite orientation (by pole density calculations) as well as lattice defects (by strain analysis) to be the main causes of the intensity differences. Our analysis of the impact of preferential orientation yields no clear relation with the observed mobility enhancement, as most of the films are preferentially oriented along the [101] or [110] directions and none of them in the direction of the lowest hole effective mass ([001]), where higher mobility is expected. On the other hand, the crystallite size and strain were extracted for all deposition conditions and we found out that the lattice strain increases with the amount of metallic tin present in the films, as observed in Figure 1e. This analysis was done by simultaneously calculating crystallite size (D) and lattice strain (ϵ) on the basis of the integral breadth (β) of the diffraction peaks by using a least-squares method to account for the β of all diffraction conditions, as explained in the experimental section. The films deposited at 7% O_{pp} , where maximum metallic tin was present (~ 5 atom %), had nearly 1 order of magnitude higher strain values (10^{-3}) than those of pure SnO (10^{-4}). The peak shift of around 0.2° in case of (200) and (211) diffraction peaks of the Sn-rich films is an indication of the strain-related intensity difference. The extracted crystallite size is about 10–15 nm for all deposition conditions tested, as confirmed by the transmission electron microscopy analysis. The higher strain values of the mixed phase films (mp-SnO) when compared to pure SnO indicate the presence of more lattice defects, which can act as potential scattering centers in the former case.

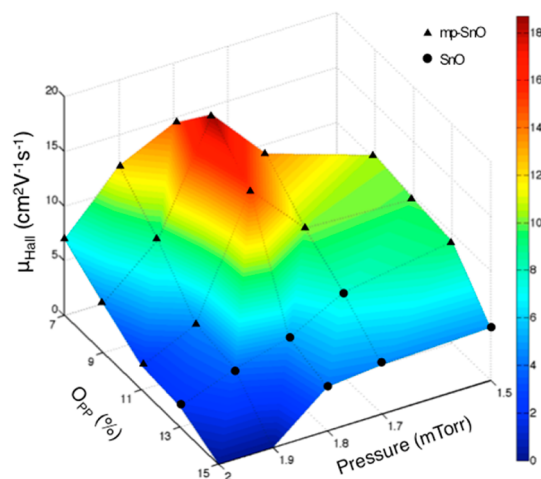


Figure 2. Room temperature Hall mobility of the films deposited in the pressure range from 1.5 to 2.0 mTorr and 7% to 15% O_{pp} . The point at 7% O_{pp} , 1.5 mTorr showing n-type conduction as well as the 15% O_{pp} at 1.9 mTorr and 2.0 mTorr showing unreliable measurements, are set to zero. A maximum Hall mobility of $18.7 \text{ cm}^2 \text{ V}^{-1} \text{ s}^{-1}$ is obtained at 1.8 mTorr, 9% O_{pp} .

Room-temperature Hall effect measurements are summarized in the three-dimensional plot depicted in Figure 2. The plot summarizes the effect of the process parameters discussed above on the Hall mobility of the films. As shown in Figure 2, films deposited in the range of $7\% \leq O_{pp} \leq 15\%$ and a deposition pressure of 1.5 to 2.0 mTorr exhibit p-type behavior (a positive Hall effect coefficient). Films processed using conditions outside this window showed n-type or metallic behavior in accordance with the phase map in Figure 1a. According to Figure 2, a maximum Hall mobility (μ_{Hall}) of $18.7 \text{ cm}^2 \text{ V}^{-1} \text{ s}^{-1}$ is obtained for the films deposited

TABLE 1. Hall Mobility, Carrier Density, and Film Conductivity As Extracted from Room Temperature Hall Effect Measurements^a

O _{pp} \ Dep. Pressure	1.5 mTorr	1.7 mTorr	1.8 mTorr	1.9 mTorr	2.0 mTorr
7%					
Mobility (cm ² /Vs)	n	9.60	14.48	12.22	7.01
Carrier Density (cm ⁻³)	n	2.42E+17	2.57E+17	3.12E+17	3.33E+17
Conductivity (S/cm)	n	0.3738	0.5986	0.6133	0.3757
9%					
Mobility (cm ² /Vs)	10.43	13.57	18.71	8.78	4.45
Carrier Density (cm ⁻³)	2.29E+17	2.38E+17	2.18E+17	2.37E+17	3.33E+17
Conductivity (S/cm)	0.3838	0.5198	0.6560	0.3350	0.2386
11%					
Mobility (cm ² /Vs)	9.83	10.16	15.21	4.45	2.25
Carrier Density (cm ⁻³)	7.55E+16	1.44E+17	7.62E+16	5.11E+16	2.31E+17
Conductivity (S/cm)	0.1195	0.2363	0.1865	0.0366	0.0836
13%					
Mobility (cm ² /Vs)	9.33	7.68	5.08	3.82	1.95
Carrier Density (cm ⁻³)	7.62E+16	1.91E+17	4.83E+16	9.77E+16	6.88E+16
Conductivity (S/cm)	0.1144	0.2359	0.0395	0.0601	0.0216
15%					
Mobility (cm ² /Vs)	4.82	4.50	4.00	X	X
Carrier Density (cm ⁻³)	7.83E+16	6.23E+16	5.90E+16	X	X
Conductivity (S/cm)	0.0607	0.0451	0.0380	X	X

Pure phase SnO
n - n-type conduction
X - high resistance

^a The reported value is the average of 3 measurements performed on different samples of every deposition condition. A maximum Hall mobility of 18.7 cm² V⁻¹ s⁻¹ is obtained at 1.8 mTorr, 9% O_{pp}.

at 1.8 mTorr and 9% O_{pp}, which surprisingly does not correspond to pure SnO films, but to the mixed phase ones (mp-SnO). The maximum μ_{Hall} obtained in this study is 8 times higher than the value reported for single-phase (001) epitaxial SnO²² and is of sufficiently large value that practical applications can be realized. The measured carrier density ranges from 4.83×10^{16} cm⁻³ to 3.33×10^{17} cm⁻³, which is in the range of previously observed p-type SnO.^{18,20,22} Details of the Hall mobility, carrier density, and film conductivity are shown in Table 1.

Figure 2 also shows that within the p-type transport process window (Figure 1a), the mobility increases as O_{pp} drops (and Sn levels increase) for several pressure values. This mobility increase occurs up to a point then begins to decrease. The O_{pp} value at which the mobility peaks depends on process pressure as shown in Figure 2. An important question to answer is how the excess metallic tin, present in the mp-SnO films, affects the hole mobility. According to our phase map (Figure 1a), a pure SnO phase is obtained with 15% O_{pp} at a deposition pressure of 1.5 mTorr and with O_{pp} \geq 13% for the other pressures. It is important to note that the films deposited under these conditions exhibit rather low μ_{Hall} values as shown in Figure 2. The role of additional metallic tin becomes clearer if we compare two films with and without detectable metal content (XRD patterns shown in Figure 1c): (i) 13% O_{pp}, 1.5 mTorr and (ii) 13% O_{pp}, 1.9 mTorr. In the former case, $\mu_{\text{Hall}} = 9.3$ cm² V⁻¹ s⁻¹, while for pure SnO, μ_{Hall} drops to 3.8 cm² V⁻¹ s⁻¹. A similar trend is observed at 1.8 mTorr process pressure for 11% O_{pp} and 13% O_{pp}, where the presence of metallic tin (Figure 1b) boosts the mobility in the 11% O_{pp} film ($\mu_{\text{Hall}} = 15.2$ cm² V⁻¹ s⁻¹). When metallic tin becomes the dominant phase, the films show n-type conduction as observed under

the 7% O_{pp}, 1.5 mTorr condition (back of Figure 2). Thus, the amount of embedded Sn must be precisely controlled to obtain high mobility. As mentioned previously, at 1.8 mTorr deposition pressure, the amount of excess Sn increased from undetectable by XPS to nearly 5 atom % as the oxygen partial pressure (O_{pp}) was reduced from 15% to 7%. At the optimum mobility point ($P = 1.8$ mTorr, O_{pp} = 9%), the Sn metal content was around 3 atom %. Finally, the phase map in Figure 1a shows that the films deposited at O_{pp} of 15% and 2 mTorr are amorphous. These films were in fact too resistive to measure, and we assumed mobility to be essentially zero.

Since the mixed phase tin monoxide films (mp-SnO) exhibit the highest Hall mobility, it is important to understand how this mixture of phases results in mobility improvement. The conduction band minima (CBM) of n-type metal oxide semiconductors are mainly formed of spatially spread s orbitals of the metal cations exhibiting large electron mobility,^{18,22} while the valence band maxima (VBM) is mainly formed of localized and anisotropic O 2p orbitals, which results in low hole mobility.³ SnO has a larger and better hole mobility owing to its hybridized orbitals, as the VBM has nearly equal contributions of the Sn 5s and O 2p orbitals.^{30,31} We believe that small traces of metal cations are advantageous to further reduce the valence band edge localization of the SnO matrix in which the VBM is made of pseudoclosed ns^2 orbitals.^{22,32} Our preliminary density functional theory simulation studies suggest that defects generated under Sn-rich growth conditions (Sn interstitial and O vacancy) give a more metallic character to the valence band of SnO. The contribution of the metal cation orbitals (particularly Sn 5p orbitals) is increased near the VBM under the presence of these defects.

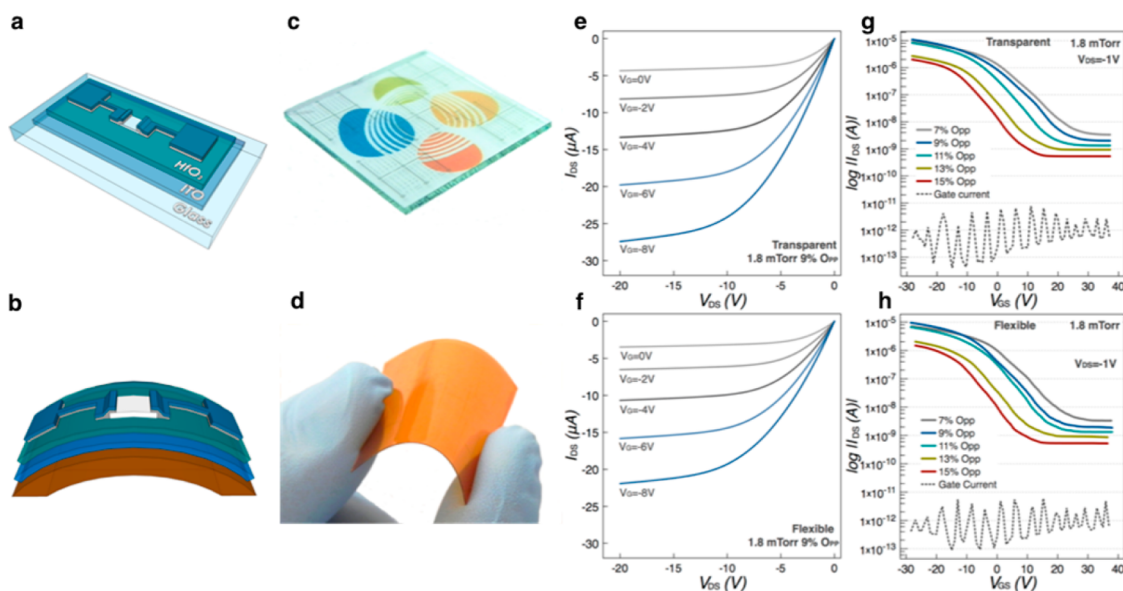


Figure 3. Conceptual designs of the fabricated devices. (a) Fully transparent devices on glass and (b) flexible devices (150 nm ITO gate electrode/220 nm HfO_2 gate dielectric/15 nm SnO active channel/8 nm Ti, 90 nm ITO source and drain electrodes). Photograph of (c) a fully transparent device and (d) a flexible one. (e,g) Output and transfer characteristics of devices fabricated on glass (fully transparent) and (f,h) devices fabricated on polyimide (flexible) with a channel width of $50\ \mu\text{m}$ and length of $50\ \mu\text{m}$. The gate currents of all the devices were around 10^{-12} amps.

Nevertheless, the amount of additional metal must be carefully controlled not to compensate the holes generated by the Sn vacancies, which give SnO its p-type character. Mobility improvement by incorporating excess Sn occurs only up to a point determined by the process conditions used, as clearly shown in Figure 2. In fact, we observe that increasing Sn metal content beyond a certain point in the mp-SnO films degrades both the Hall and field-effect mobility (e.g., 7% O_{PP} films). We believe that this result is due to the fact that further increasing the Sn metal concentration increases carrier scattering and therefore reduces hole mobility. The presence of metallic tin can contribute to carrier scattering in several ways. For instance, too much tin can introduce additional point defects (e.g., additional Sn interstitials in the SnO lattice, free Sn atoms and clusters in the grain boundaries, or dislocations) that act to scatter the charge carriers. It is evident that more defects are introduced in mixed phase films with higher content of metallic Sn as presented in the lattice strain analysis (Figure 1e). This analysis was done by simultaneously calculating crystallite size (D) and lattice strain (ϵ) on the basis of the integral breadth (β) of the diffraction peaks by using a least-squares method to account for the β of all diffraction conditions. Basically, we find that the pure phase SnO films (lower right-hand side of Figure 1e) exhibited lower strain compared to mp-SnO films. In contrast, mp-SnO films with high levels of metallic tin (upper left-hand side of Figure 1e) exhibit higher strain levels, indicating a larger concentration of defects in the films (e.g., Sn interstitials in the SnO lattice, free Sn atoms, and clusters in the grain boundaries,

dislocations). These defects, if present in significant amounts, can enhance carrier scattering, leading to a decrease in hole mobility. Therefore, the optimum mobility in our tin monoxide films is determined by a trade-off between (i) the extent of valence band modulation caused by additional metal cations, and (ii) the amount of charge carrier scattering from defects induced by the presence of increasing amounts of metallic tin in the mp-SnO films.

Device Characterization. The conceptual design of the fully transparent and flexible devices is depicted in Figure 3 panels a and b, whereas Figure 3 panels c and d show the actual fabricated devices. Figure 3 panels e and f depict the output characteristics of fully transparent and flexible devices produced at 9% O_{PP} , $P = 1.8\ \text{mTorr}$, respectively, in which clear linear and saturation regions can be observed. The absence of current crowding at low source-to-drain voltages (V_{DS}) indicates an Ohmic contact of Ti/ITO with SnO. Figure 3 panels g and h present the transfer characteristics measured with $V_{DS} = -1\ \text{V}$ for devices produced at 1.8 mTorr with different O_{PP} . In all cases, p-type behavior is observed, since the holes are generated at negative gate voltages (V_{GS}). Figure 3 panels g and h also show that the gate leakage currents are very low and are around 10^{-12} amps. Linear-region field-effect mobility (μ_{FE}) and threshold voltage (V_T) were calculated from the transfer characteristics and the obtained values are shown in Figure 4 panels a and b, respectively. To rule out any artifacts in the TFT measurements, all the devices were characterized following the procedure recommended by J.F. Wager³³ with multiple W/L ratios. The mobility data shown in Figure 4a were

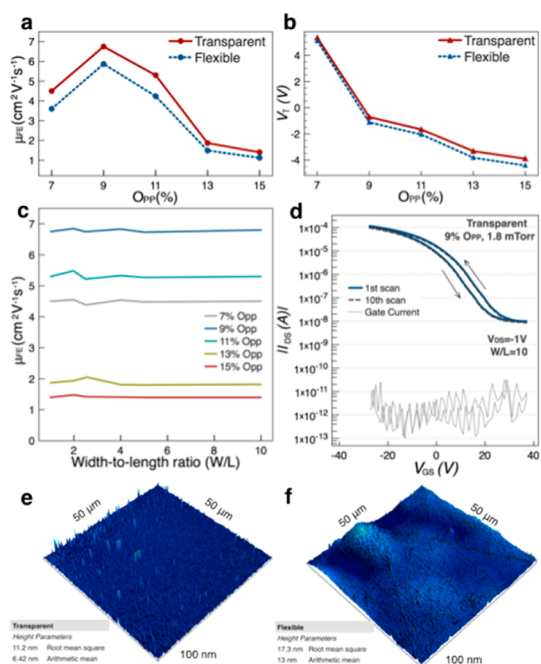


Figure 4. (a) Linear field-effect mobility (μ_{FE}) as a function of O_{PP} for the devices fabricated for this study at $P = 1.8$ mTorr. (b) Threshold voltage (V_T) comparison of the fully transparent and flexible devices. (c) Linear field-effect mobility as a function of width-to-length ratio for the transparent samples. (d) Multiple, dual-sweep transfer curves for a device with a $W/L = 10$ at the best performance condition (9% O_{PP} , 1.8 mTorr). (e, f) AFM surface profiles for the mp-SnO films deposited on glass and polyimide substrates, respectively.

extracted from devices with $W/L = 1$, but W/L ratios from 1 to 10 were tested and gave very similar results as shown in Figure 4c for the set of fully transparent devices. Multiple, dual sweep I_{DS} vs V_{GS} scans were performed, and it was found that the devices belong to type II in Wager's classification³³ which is *nonequilibrium, steady-state behavior*. An effective hysteresis density of $N_{HYS} = 1.8645 \times 10^{12} \text{ cm}^{-2}$ with a threshold voltage shift of 3.67 V at a V_{GS} scan rate $SR = 366 \text{ mV/s}$ is observed for the best performance device (9% O_{PP} , 1.8 mTorr) as shown in Figure 4d with a W/L ratio of 10. The transparent TFTs on glass have a maximum μ_{FE} of $6.75 \text{ cm}^2 \text{ V}^{-1} \text{ s}^{-1}$ while the mobility is nearly 20% lower for the TFTs made on flexible substrates. Results of SnO surface inspection by atomic force microscopy using the same area as in actual devices ($50 \mu\text{m} \times 50 \mu\text{m}$) are presented in Figure 4 panels e and f for glass and plastic substrates, respectively. It is evident that the mixed phase (mp-SnO) films deposited on flexible substrates have a higher surface roughness. The lower mobility of devices on flexible polyimide substrate can thus be attributed to the higher surface roughness of this substrate, which increases carrier scattering and hence reduces the mobility. The threshold voltage (V_T) of the flexible devices matches well with the V_T of the rigid ones. The gate leakage current in the on state was measured in the pA range, indicating good insulating properties of the dielectric layer. For all O_{PP} conditions,

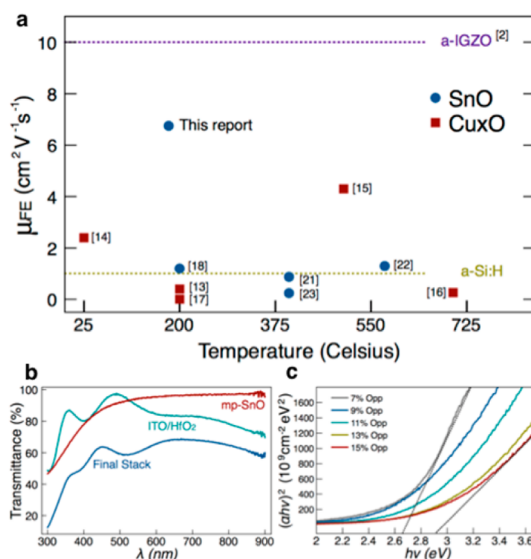


Figure 5. (a) Comparison of reported field-effect mobility versus maximum processing temperature (either deposition or post annealing) for leading p-type oxides. The reference is indicated in square brackets. Mobility of a-IGZO (n-type) and a-Si:H are not plotted as a function of the temperature and are used just for comparison. (b) Transmission spectra of the components of the TFT. (c) Tauc plot of the optical band gap extraction (indicated by the dotted line) of the films deposited at 1.8 mTorr.

the I_{ON}/I_{OFF} ratio is around 10^3 , leading to a maximum of 6×10^3 for the device with highest mobility.

As expected, devices produced at different O_{PP} exhibit different behaviors. μ_{FE} follows a similar trend to that of μ_{Hall} shown in Figure 2. The hole mobility reaches its maximum in case of devices (and films) deposited at 9% O_{PP} , 1.8 mTorr, which corresponds to the mp-SnO films with ~ 3 atom % Sn. Competing contributions of metal cations are also observed in our devices: TFTs fabricated with mp-SnO films have higher mobility than those fabricated with pure SnO. It is obvious that the presence of small amounts of Sn enhances hole mobility by promoting orbital delocalization in the valence band, but this delocalization has to be controlled so that the scattering effects do not cancel out the mobility enhancement. The shift of V_T as a function of O_{PP} also gives an indication of the crucial role of the embedded metallic Sn. V_T is positive for 7% O_{PP} , then becomes negative and further decreases as the Sn concentration decreases (or the SnO phase becomes dominant) with a value of -1 V for the best-performing device. TFTs fabricated at 7% O_{PP} , when more metallic Sn is present, exhibit a positive V_T , indicating the presence of large number of free carriers. As O_{PP} increases from 9% to 15%, a significant decrease in I_{DS} is observed, indicating a decrease in carrier concentration (as seen in Table 1), as is also evident from the shifting of V_T in the negative direction.

The TFT data correlate very well with the Hall mobility data, although the actual μ_{FE} is smaller than μ_{Hall} regardless of the deposition conditions. This is

typical behavior for oxide semiconductors and likely arises from defects near the valence band maximum and/or hole traps at the semiconductor–dielectric interface. Extracted subthreshold swing data in the range from 7.63 V dec^{-1} to 10 V dec^{-1} indicate that there is a high density of trap states in the semiconductor and/or at the interface with the dielectric. Optimization of the semiconductor–dielectric interface has been shown to play a crucial role in maximizing device performance.³⁴ Better device engineering to decrease the number of trap states should allow the μ_{FE} to approach μ_{Hall} more closely. We note here that our field-effect mobility stands out as the highest reported up-to-date for any p-type transparent oxide semiconductor, as shown in Figure 5a where the two most promising p-type oxides are compared.

The transmittance spectra of the gate electrode and the gate dielectric, the mp-SnO layer, and the final stack are shown in Figure 5b. The average optical transmission of the 15 nm mp-SnO layer in the visible region (400–700 nm) is 92%, while it is 63% for the entire device, mainly limited by the Ti layer. The use of the Ti source and drain contact interlayer results from the observation of enhanced device performance over some other contacts like Au, Ni, Pt, and ITO. The optical

bandgap, E_{G} , has been estimated from the absorption coefficient, α , calculated as a function of the incident photon energy, $h\nu$. E_{G} was obtained by extrapolating the linear portion in the $(\alpha h\nu)^2$ vs $h\nu$ plot, as shown in Figure 5c by the dotted lines. The estimated E_{G} ranges from 2.65 eV for 7% O_{PP} to 2.92 eV for 15% O_{PP}, matching well with that of pure SnO.^{19,22}

CONCLUSIONS

We have demonstrated the highest hole mobility reported to date for a p-type oxide processed at low temperature by careful process control. A detailed phase map for nanoscale physical vapor deposition of tin monoxide has been developed for the first time. We have shown that control of the phase formation of tin monoxide films greatly enhances the carrier mobility yielding $\mu_{\text{Hall}} = 18.7 \text{ cm}^2 \text{ V}^{-1} \text{ s}^{-1}$. Residual second phases must be carefully optimized to obtain maximum hole mobility. Furthermore, we have demonstrated record device performance for a transparent p-type oxide semiconductor on both rigid and flexible substrates, with a linear-region field-effect mobility of $6.75 \text{ cm}^2 \text{ V}^{-1} \text{ s}^{-1}$ and $5.87 \text{ cm}^2 \text{ V}^{-1} \text{ s}^{-1}$, respectively, a threshold voltage of -1 V and an $I_{\text{ON}}/I_{\text{OFF}}$ ratio of 6×10^3 .

METHODS

Film Fabrication and Characterization. Pure SnO and mixed phase (mp-SnO) films were deposited onto soda-lime glass substrates by direct current (DC) reactive magnetron sputtering using a 2 in. (5.08 cm) tin metal target from Angstrom Science, Canada, with a purity of 99.99%. The reactive sputtering was performed at room temperature in a mixture of argon and oxygen gases, in an AMOD-model thin film deposition tool designed by Angstrom Engineering. To determine optimal deposition conditions, the oxygen partial pressure was varied from 3% to 50%. The deposition pressure was scanned from 1 to 4 mTorr while the DC power was held at 30 W (9.55 W/in² power density). The distance between the target and the substrate was 20 cm, while the gun is located at 160° with respect to the horizon, achieving a deposition rate of 0.8 \AA/s . Post-annealing in air was performed in a tube furnace at 180°C for 30 min. The film thicknesses were measured using a Veeco Dektak 150 surface profilometer and confirmed by cross-sectional transmission electron microscopy (TEM) analysis performed with a FEI Titan ST. High-resolution X-ray diffraction patterns were obtained at room temperature in air by a Bruker D8 Discover diffractometer using the $\text{CuK}\alpha_1$ (1.5406 Å) radiation. Carrier density and Hall mobility were extracted from room temperature Hall effect measurements conducted using a physical property measurement system (PPMS) from Quantum Design in a Greek-cross patterned film with the Van der Pauw configuration and after magnetoresistance correction. The optical properties were obtained using an evolution 600 UV–vis spectrophotometer in the wavelength range from 300 to 900 nm. Surface morphologies were imaged by an Agilent 5400 SPM AFM system and FEI Helios NanoLab 400S SEM. Crystallite size (D) and lattice strain (ε) were simultaneously calculated on the basis of the integral breadth (β) of the diffraction patterns by using a least-squares method to account for the β of all diffraction conditions according to eq 1.²⁷

$$\beta_{\text{t}} \approx \left(\frac{0.9\lambda}{D \cos\theta} \right)^2 + (4\varepsilon \tan\theta)^2 + \beta_{\text{o}}^2 \quad (1)$$

where λ is the $\text{CuK}\alpha_1$ line and β_{o} is the instrumental broadening. At least six SnO diffraction conditions were observed for all the deposition conditions, as seen in Figure 1b. Using a MATLAB routine, the integral breadth, defined as the total area under the peak divided by the peak height, was obtained for the observed SnO diffraction conditions. With the obtained values and using eq 1, equal number of eqs (6 to 7) with three unknowns (D , ε and β_{o}) were formed and solved using a least-squares method in MATLAB.

TFT Fabrication and Characterization. The bottom gate indium tin oxide (ITO) layers were deposited by radio frequency magnetron sputtering at room temperature. The HfO_2 (220 nm) gate dielectric was deposited on top of 150 nm ITO-coated glass/polyimide substrates by atomic layer deposition using a Cambridge Nanotech system. The active layer consisted of 15 nm of SnO deposited at different oxygen partial pressures. The stack was completed with 8 nm electron-beam evaporated Ti and 90 nm sputtered ITO source and drain contacts followed by thermal treatment at 180°C in air, for 30 min, to crystallize both the SnO and ITO layers. The devices were patterned by photolithography and lift-off technique and measured on a probe station in air using a Keithley 4200-SCS semiconductor parameter analyzer at room temperature in the dark. The performance of the TFTs was evaluated on devices with a width-to-length ratio (W/L) of 1 having W and L of $50 \mu\text{m}$, respectively. Linear-region field-effect mobility (μ_{FE}), threshold voltage (V_{T}) and subthreshold swing (S) were evaluated with the conventional metal-oxide–semiconductor field effect transistor model described in eqs 2 and 3

$$I_{\text{DS}} = \mu C_{\text{ox}} \frac{W}{L} \left[(V_{\text{GS}} - V_{\text{T}}) V_{\text{DS}} - \frac{V_{\text{DS}}^2}{2} \right] \quad \text{for } V_{\text{DS}} < V_{\text{GS}} - V_{\text{T}} \quad (2)$$

where C_{ox} is the capacitance per unit area of the gate insulator and measured to be 60 nFcm^{-2} with no more than 3% variation in the frequency range from 1 kHz to 1 MHz and

an extracted dielectric constant of ≈ 14 .

$$S = \frac{dV_{GS}}{d(\log I_{DS})} \approx \ln 10 \frac{kT}{q} \left[1 + \frac{qC_d}{C_{ox}} \right] \quad (3)$$

Conflict of Interest: The authors declare no competing financial interest.

Acknowledgment. The authors thank Dongkyu Cha for the TEM and SEM images and Nejib Hedhili for the XPS measurements. J. A. Caraveo-Frescas thanks the KAUST nanofabrication and thin film facilities personnel for their support. H. N. Alshareef acknowledges the generous support of the KAUST baseline fund.

REFERENCES AND NOTES

- Sun, Y.; Rogers, J. A. Inorganic Semiconductors for Flexible Electronics. *Adv. Mater.* **2007**, *19*, 1897–1916.
- Nomura, K.; Ohta, H.; Takagi, A.; Kamiya, T.; Hirano, M.; Hosono, H. Room-Temperature Fabrication of Transparent Flexible Thin-Film Transistors Using Amorphous Oxide Semiconductors. *Nature* **2004**, *432*, 484–492.
- Kykyneshi, R.; Zeng, G.; Cann, D. P., Transparent Conducting Oxides Based on Tin Oxide. In *Handbook of Transparent Conductors*; Ginley, D. S., Hosono, H., Paine, D. C., Eds.; Springer: New York, 2010; pp 171–191.
- Kim, B.; Hyung Nyuck, C.; Woo Seok, C.; Seung-Hee, K.; Yong, Ho, J.; Juhn-Suk, Y.; Soo Young, Y.; Myungchul, J.; Yong-Kee, H.; Min-Koo, H. Highly Reliable Depletion-Mode a-IGZO TFT Gate Driver Circuits for High-Frequency Display Applications Under Light Illumination. *IEEE Electron Device Lett.* **2012**, *33*, 528–530.
- Kim, K. M.; Kim, C. W.; Heo, J.-S.; Na, H.; Lee, J. E.; Park, C. B.; Bae, J.-U.; Kim, C.-D.; Jun, M.; Hwang, Y. K.; *et al.* Competitive Device Performance of Low-Temperature and All-Solution-Processed Metal-Oxide Thin-Film Transistors. *Appl. Phys. Lett.* **2011**, *99*, 242109–1–242109–3.
- Fortunato, E.; Barquinha, P.; Martins, R. Oxide Semiconductor Thin-Film Transistors: A Review of Recent Advances. *Adv. Mater.* **2012**, *24*, 2945–2986.
- Reuss, R. H.; Chalamala, B. R.; Mousseian, A.; Kane, M. G.; Kumar, A.; Zhang, D. C.; Rogers, J. A.; Hatalis, M.; Temple, D.; Moddel, G.; *et al.* Macroelectronics: Perspectives on Technology and Applications. *Proc. IEEE* **2005**, *93*, 1239–1256.
- Kim, M.-G.; Kanatzidis, M. G.; Facchetti, A.; Marks, T. J. Low-Temperature Fabrication of High-Performance Metal Oxide Thin-Film Electronics via Combustion Processing. *Nat. Mater.* **2011**, *10*, 382–388.
- Arias, A. C.; MacKenzie, D. J.; McCulloch, I.; Rivnay, J.; Salleo, A. Materials and Applications for Large Area Electronics: Solution-Based Approaches. *Chem. Rev.* **2010**, *110*, 3–24.
- Fortunato, E. M. C.; Barquinha, P. M. C.; Pimentel, A. C. M. B. G.; Gonçalves, A. M. F.; Marques, A. J. S.; Pereira, L. M. N.; Martins, R. F. P. Fully Transparent ZnO Thin-Film Transistor Produced at Room Temperature. *Adv. Mater.* **2005**, *17*, 590–594.
- Kim, H. S.; Byrne, P. D.; Facchetti, A.; Marks, T. J. High Performance Solution-Processed Indium Oxide Thin-Film Transistors. *J. Am. Chem. Soc.* **2008**, *130*, 12580–12581.
- Nayak, P. K.; Hedhili, M. N.; Cha, D. K.; Alshareef, H. N. High Performance Solution-Deposited Amorphous Indium Gallium Zinc Oxide Thin Film Transistors by Oxygen Plasma Treatment. *Appl. Phys. Lett.* **2012**, *100*, 202106–1–202106–4.
- Sung, S.-Y.; Kim, S.-Y.; Jo, K.-M.; Lee, J.-H.; Kim, J.-J.; Kim, S.-G.; Chai, K.-H.; Pearson, S. J.; Norton, D. P.; Heo, Y.-W. Fabrication of p-Channel Thin-Film Transistors Using CuO Active Layers Deposited at Low Temperature. *Appl. Phys. Lett.* **2010**, *97*, 222109–1–222109–3.
- Yao, Z. Q.; Liu, S. L.; Zhang, L.; He, B.; Kumar, A.; Jiang, X.; Zhang, W. J.; Shao, G. Room Temperature Fabrication of p-Channel Cu₂O Thin-Film Transistors on Flexible Polyethylene Terephthalate Substrates. *Appl. Phys. Lett.* **2012**, *101*, 042114–1–042114–4.
- Zou, X.; Guojia, F.; Longyan, Y.; Meiya, L.; Wenjie, G.; Xingzhong, Z. Top-Gate Low-Threshold Voltage p-Cu₂O Thin-Film Transistor Grown on SiO₂/Si Substrate Using a High-k HfON Gate Dielectric. *IEEE Electron Device Lett.* **2010**, *31*, 827–829.
- Matsuzaki, K.; Nomura, K.; Yanagi, H.; Kamiya, T.; Hirano, M.; Hosono, H. Epitaxial Growth of High Mobility Cu₂O Thin Films and Application to p-Channel Thin Film Transistor. *Appl. Phys. Lett.* **2008**, *93*, 202107–1–202107–3.
- Fortunato, E.; Figueiredo, V.; Barquinha, P.; Elamurugu, E.; Barros, R.; Goncalves, G.; Park, S.-H. K.; Hwang, C.-S.; Martins, R. Thin-Film Transistors Based on p-type Cu₂O Thin Films Produced at Room Temperature. *Appl. Phys. Lett.* **2010**, *96*, 192102–1–192102–3.
- Fortunato, E.; Barros, R.; Barquinha, P.; Figueiredo, V.; Park, S.-H. K.; Hwang, C.-S.; Martins, R. Transparent p-type SnO_x Thin Film Transistors Produced by Reactive rf Magnetron Sputtering Followed by Low Temperature Annealing. *Appl. Phys. Lett.* **2010**, *97*, 052105–1–052105–3.
- Guo, W.; Fu, L.; Zhang, Y.; Zhang, K.; Liang, L. Y.; Liu, Z. M.; Cao, H. T.; Pan, X. Q. Microstructure, Optical, and Electrical Properties of p-type SnO Thin Films. *Appl. Phys. Lett.* **2010**, *96*, 042113–1–042113–3.
- Lee, H.-N.; Kim, H.-J.; Kim, C.-K. p-Channel Tin Monoxide Thin Film Transistor Fabricated by Vacuum Thermal Evaporation. *Jpn. J. Appl. Phys.* **2010**, *49*, 020202–1–020202–3.
- Liang, L. Y.; Liu, Z. M.; Cao, H. T.; Xu, W. Y.; Sun, X. L.; Luo, H.; Cang, K. The Structural, Optical and Electrical Properties of Y-doped SnO Thin Films and Their p-Type TFT Application. *J. Phys. D: Appl. Phys.* **2012**, *45*, 085101–1–085101–5.
- Ogo, Y.; Hiramatsu, H.; Nomura, K.; Yanagi, H.; Kamiya, T.; Hirano, M.; Hosono, H. p-Channel Thin-Film Transistor Using p-Type Oxide Semiconductor, SnO. *Appl. Phys. Lett.* **2008**, *93*, 032113–1–032113–3.
- Yabuta, H.; Kaji, N.; Hayashi, R.; Kumomi, H.; Nomura, K.; Kamiya, T.; Hirano, M.; Hosono, H. Sputtering Formation of p-Type SnO Thin-Film Transistors on Glass Toward Oxide Complimentary Circuits. *Appl. Phys. Lett.* **2010**, *97*, 072111–1–072111–3.
- Batzill, M.; Diebold, U. The Surface and Materials Science of Tin Oxide. *Prog. Surf. Sci.* **2005**, *79*, 47–154.
- Pan, X. Q.; Fu, L. Oxidation and Phase Transitions of Epitaxial Tin Oxide Thin Films on (1-bar 012) Sapphire. *J. Appl. Phys.* **2001**, *89*, 6048–6055.
- Geurts, J.; Rau, S.; Richter, W.; Schmitte, F. J. SnO Films and Their Oxidation to SnO₂: Raman Scattering, IR Reflectivity, and X-ray Diffraction Studies. *Thin Solid Films* **1984**, *121*, 217–225.
- Birkholz, M. *Thin-Film Analysis by X-ray Scattering*; Wiley-VCH: Weinheim, Germany, 2006.
- Ramadan, A. A.; Abd El-Mongy, A. A.; El-Shabiny, A. M.; Mater, A. T.; Mostafa, S. H.; El-Sheehedy, E. A.; Hashem, H. M. Addressing Difficulties in Using XRD Intensity for Structural Study of Thin Films. *Crys. Res. Technol.* **2009**, *44*, 111–116.
- Delhez, R.; Keijsers, T. H.; Mittemeijer, E. J. Determination of Crystallite Size and Lattice Distortions through X-ray Diffraction Line Profile Analysis. *Fresenius Z. Anal. Chem.* **1982**, *312*, 1–16.
- Togo, A.; Oba, F.; Tanaka, I.; Tatsumi, K. First-Principles Calculations of Native Defects in Tin Monoxide. *Phys. Rev. B* **2006**, *74*, 195128–1–195128–8.
- Watson, G. W. The Origin of The Electron Distribution in SnO. *J. Chem. Phys.* **2001**, *114*, 758–763.
- Ogo, Y.; Hiramatsu, H.; Nomura, K.; Yanagi, H.; Kamiya, T.; Kimura, M.; Hirano, M.; Hosono, H. Tin Monoxide as an s-Orbital-Based p-type Oxide Semiconductor: Electronic Structures and TFT Application. *Phys. Status Solidi A* **2009**, *206*, 2187–2191.
- Wager, J. F. Transfer-Curve Assessment of Oxide Thin-Film Transistors. *J. Soc. Inf. Disp.* **2010**, *18*, 749–752.
- Lee, C.-G.; Dodabalapur, A. Solution-Processed Zinc-Tin Oxide Thin-Film Transistors with Low Interfacial Trap Density and Improved Performance. *Appl. Phys. Lett.* **2010**, *96*, 243501–1–243501–3.